Optimizing Coverage with Intelligent Surfaces for Indoor mmWave Networks

Jingyuan Zhang and Douglas M. Blough School of Electrical and Computer Engineering Georgia Institute of Technology, USA {jingyuan, doug.blough }@ece.gatech.edu

Abstract—Reconfigurable intelligent surfaces (RISs) have been proposed to increase coverage in millimeter-wave networks by providing an indirect path from transmitter to receiver when the line-of-sight (LoS) path is blocked. In this paper, the problem of optimizing the locations and orientations of multiple RISs is considered for the first time. An iterative coverage expansion algorithm based on gradient descent is proposed for indoor scenarios where obstacles are present. The goal of this algorithm is to maximize coverage within the shadowed regions where there is no LoS path to the access point. The algorithm is guaranteed to converge to a local coverage maximum and is combined with an intelligent initialization procedure to improve the performance and efficiency of the approach. Numerical results demonstrate that, in dense obstacle environments, the proposed algorithm doubles coverage compared to a solution without RISs and provides about a 10% coverage increase compared to a brute force sequential RIS placement approach.

Index Terms—Intelligent surface, millimeter-wave communication, coverage, RIS location and orientation optimization

I. INTRODUCTION

The conflict between limited spectrum resources and explosive demands for data services has generated strong interest in higher frequency bands for fifth-generation (5G) and beyond 5G communications, among which millimeterwave (mmWave) wireless communication is one of the most promising alternatives. Due to the scarcity of current spectrum resources, the large bandwidth available in the 30–300 GHz mmWave band brings the opportunity for ultra-high demands to be met within that band [1] [2]. Despite the promising benefits, the deployment of mmWave communication faces challenges including severe path loss and penetration loss caused by blockages. In an indoor scenario, walls and furniture can cause severe coverage problems for mmWave networks [3].

To overcome this issue, reconfigurable intelligent surfaces (RISs) [4] (also known as intelligent reflecting surfaces (IRSs) [5] or software-defined meta-surfaces [6]) have been proposed to expand transmission coverage in the mmWave bands [6]. Intelligent surfaces are composed of an array of electromagnetic elements, which are nearly passive and do not require RF chain components including power amplifiers and analog-to-digital/digital-to-analog converters so that their energy requirements are low [7]. Meanwhile, the electromagnetic characteristics of each element can be reconfigured to interact with incident waves and manipulate reflected waves for various functionalities. In the mmWave band, RISs can be deployed to establish extra links between transmitter and

receiver when there is no line-of-sight (LoS) path between them with the advantage of low power consumption compared with conventional approaches such as multi-antenna relays, which makes them a promising way to handle the coverage issue in mmWave communication [8]–[11].

Though potential of RISs to expand coverage has been widely studied, the problem of how to optimize RIS deployment still remains an open problem. The novel problem considered herein is optimization of coverage based on multi-RIS deployment in a scenario with fixed obstacles. The challenges of this problem include multi-agent optimization, for which it is difficult to find optimal solutions considering realistic factors including obstacles and RIS radiation patterns. This paper presents a gradient-descent-based algorithm to optimize locations and orientations of RISs, which is inspired by coverage control algorithms in multi-robot systems [12]-[15]. The objective of this algorithm is to maximize a coverage performance function by iteratively updating both position and orientation of each RIS. The performance function is carefully selected to reflect the anisotropic coverage performance caused by the radiation pattern of RIS elements. In addition, it is guaranteed to provide a local optimum in an indoor scenario with obstacles. Since the performance of gradient descent algorithms is sensitive to initial states when the objective function is non-convex, an initialization method is also proposed to reach better coverage performance efficiently.

The rest of the paper is organized as follows. Section II summarizes existing researches related to the topic. Section III introduces the formulation of the RIS optimization problem. A detailed presentation of the proposed RIS optimization algorithm is given in Section IV. Numerical simulation is presented in Section V to validate the proposed algorithm. Finally, Section VI concludes the paper.

II. RELATED WORK

Most prior work on RIS coverage issues has focused on RIS phase shift design given fixed RIS locations. In [16], an RIS placed on a building is used to provide extra links between unmanned aerial vehicles (UAVs) and ground users. Therein, RIS beamforming vector and UAV trajectory are jointly designed with the aim to maximize average achievable rate. In [17], joint optimization for access point (AP) beamforming and RIS passive beamforming has been proposed in multi-user systems based on a practical phase shift model. Furthermore,

deep-learning-based approaches are also employed to design the RIS phase matrix in [18] [19].

Despite extensive studies on coverage issues assisted by RISs, there has not been much work on practical RIS deployment. There are some existing works that concentrate on optimizing a single RIS placement. In [20], the authors analyze the optimal location of a single RIS in a simple scenario with a single antenna transmitter and receiver. The optimal horizontal distance between RIS and receiver derived in this paper indicates that the RIS should be close to either the transmitter or the receiver. The placement of a single RIS is analyzed in three-dimensional environments in [21]. In [22], a coverage maximization algorithm is given to find optimized location and orientation of a single RIS given one base station and one user. The authors focus on extending the cell radius, and thus do not take obstacles into consideration. In [23], the authors discuss optimal placement of one RIS given fixed locations of one transmitter and one receiver in a mmWave link in order to maximize end-to-end SNR. In [24], the authors propose that cellular network coverage can be extended by deploying RISs at the edges of cells for aerial users, with the intention to maximize signal-to-interference-plus-noise ratio and mitigate inter-cell interference.

Despite initial discussions on RIS deployment, the above works do not demonstrate the impact of realistic constraints such as obstacles on RIS deployment strategies. Some other works have tried to tackle this issue. The authors of [25] limit RIS locations in a given area and then jointly optimize location and reflection coefficients of a single RIS to maximize the sum rate of a multi-user group. In [26], a reinforcement learning framework is employed to handle the above issue. The objective is to optimize energy efficiency by jointly designing a single RIS position and phase shift based on users' data demands. However, to our knowledge, how to jointly optimize positions and orientations of multiple RISs in a realistic indoor scenario considering obstacles for coverage maximization has not been addressed previously.

III. PROBLEM FORMULATION

In this section, a problem formulation of RIS deployment optimization is presented to improve coverage performance. Some basic notations and assumptions used in this paper are also presented.

Let $\hat{\boldsymbol{v}}(\alpha) = [\cos(\alpha), \sin(\alpha)]^T$ denote a normalized vector. Let $\boldsymbol{R}(\theta) \in \mathbb{R}^{2 \times 2}$ denote a rotation matrix that rotates a vector counterclockwise by θ , i.e.

$$\mathbf{R}(\theta) = \begin{bmatrix} \cos \theta & -\sin \theta \\ \sin \theta & \cos \theta \end{bmatrix}. \tag{1}$$

An RIS is characterized by its location $q_i \in \mathbb{R}^{2\times 1}$, and orientation $\theta_i \in [-\pi, \pi]$ which is the angle between the heading direction of the *i*th RIS and positive X-axis. Then the state of each RIS is denoted by $s_i = [q_i^T, \theta_i]^T$. Let

 $\theta(s_i, p) \in [0, \pi]$ be the angle between RIS orientation θ_i and the direction from RIS location q_i to point p, such that

$$\theta(\mathbf{s}_i, \mathbf{p}) = \cos^{-1}\left(\frac{(\cos \theta_i, \sin \theta_i)(\mathbf{p} - \mathbf{q}_i)}{\|\mathbf{p} - \mathbf{q}_i\|}\right). \tag{2}$$

And let $\theta_{q_i}(p) \in [-\pi, \pi]$ represent the angle between positive X-axis and orientation from location q_i to p.

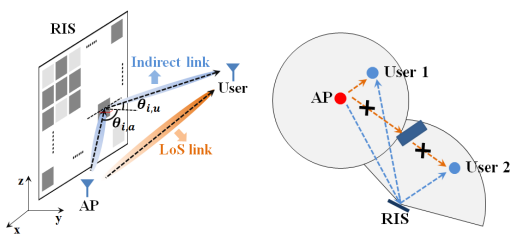
A. System Model

We consider a down-link scenario with two types of links as shown in Fig. 1(a): LoS links from AP to users, and indirect links where RISs reflect signals to users. A user will connect to the AP by either of the two links depending on channel conditions when both links can provide communication service as is the case for User 1 in Fig. 1(b). When the LoS link is blocked by obstacles or the user is out of the communication range of the AP, as for User 2 in Fig. 1(b), only the indirect path is utilized.

For simplicity, we consider a 2D case where the AP, the users, and the centers of RISs are placed on the same X-Y plane. Also it is assumed that the AP and users are all equipped with single-antenna. The RIS can be modeled as a $\sqrt{N} \times \sqrt{N}$ array where N is the number of RIS elements. Each of its elements can manipulate electromagnetic wave by adjusting the complex reflection coefficient $\tau_i = e^{j\phi_i}$, where ϕ_i is the phase shift of the ith element. Let $G_{ris}(\theta)$ denote the radiation pattern of RIS element corresponding to angle θ . It is assumed that RISs are located in the far-field region of the AP, and only the far-field case is considered when analyzing coverage performance of RISs. This is a reasonable model for evaluating coverage since the edges of the communication region determine the coverage and they typically lie in the farfield region. Moreover, reflections from obstacles and walls are neglected in this paper because those non-line-of-sight paths typically have much lower signal strength than line-of-sight or RIS-reflected paths in the mmWave bands.

B. Path Loss Model

We consider path loss models of both indirect links and LoS links. Let P_t , G_a , G_u denote the transmit power, the antenna gain of the AP, and the antenna gain of users, respectively. The path loss for an LoS link is straightforward and the received power is given by $P_{r,los} = (\frac{P_t G_a}{4\pi r_{los}^2})(\frac{\lambda^2 G_u}{4\pi})$, where λ is the



(a) System illustration (b) Top view of the system

Fig. 1. A RIS-aided communication system.

wavelength of carrier frequency, and r_{los} is the distance from the AP to the user.

Next, the path loss model of indirect links is introduced. From [27], the power transmitted to the *i*th RIS element and then received by the user is given by

$$P_r^i = \left(\frac{P_t G_a}{4\pi r_{i,a}^2} A_r\right) \left(\frac{\|\tau_i\|^2 G_{ris}(\theta_{i,u})}{4\pi r_{i,u}^2} \frac{\lambda^2 G_u}{4\pi}\right), \quad (3)$$

where A_r represents the aperture of one RIS element which, following [27], is modeled by $A_r = \frac{\lambda^2 G_{ris}(\theta_{i,a})}{4\pi}$, and $\theta_{i,a}$ and $\theta_{i,u}$ are the incident angle and the reflected angle with respect to the *i*th RIS element as illustrated in Fig.1(a). Moreover, $r_{i,a}$ and $r_{i,u}$ are distances from the AP to the ith RIS element and from the ith RIS element to the user, respectively. Then, the total received power at the user is

$$P_{r} = \left\| \sum_{i=1}^{N} \sqrt{P_{r}^{i}} e^{-j\frac{2\pi}{\lambda}(r_{i,a} + r_{i,u})} e^{j\phi_{i}} \right\|^{2}. \tag{4}$$

Under the assumption of perfect channel knowledge at the RIS [29] [30] [31], P_r can be maximized by setting the phase shift of the *i*th element as $\phi_i = \frac{2\pi}{\lambda}(r_{i,a} + r_{i,u})$ based on the assumption of continuous phase. However, RIS elements in practical systems usually have discrete phases. The phase of a b-bit RIS element can be set as $\frac{2\pi}{2^b}K$, where K is an integer that $K \in [0, 2^b - 1]$. Based on conclusions in [32], the average received power with b-bit RIS phase shifts is

$$\frac{P_r(b)}{P_r(\infty)} = \frac{16 + (N-1)\pi^2(\frac{2^b}{\pi}\sin(\frac{\pi}{2^b}))^2}{16 + (N-1)\pi^2},\tag{5}$$

where $P_r(\infty)$ is the received power corresponding to continuous phases. Since discrete phases only introduce a constant scaling factor to the received power, it will not have impact on the algorithm introduced in this paper which can be extended to discrete phases by adding the scaling factor. As a result of that, it is assumed that RISs have ideal continuous phases in this paper for simplicity. Since the far-field case is assumed, we have $r_{i,a} \approx r_{ra}$ and $r_{i,u} \approx r_{ru}$, where r_{ra} and r_{ru} are the distance from the AP to the center of RIS and the distance from the center of RIS to the user, respectively. Also, $G_{ris}(\theta_{i,u}) \approx G_{ris}(\theta_u)$ and $G_{ris}(\theta_{i,a}) \approx G_{ris}(\theta_a)$ where θ_u is the incident angle from AP to the center of RIS, and θ_a is the reflected angle from the center of RIS to the user. Then the approximation of the maximized received power is

$$P_{r,indirect} = \frac{P_t G_a G_u \lambda^4 G_{ris}(\theta_u) G_{ris}(\theta_a) N^2}{(4\pi)^4 r_{ra}^2 r_{ru}^2}.$$
 (6)

¹Another aperture model taking the size of RIS elements into consideration is $A_r = d_x d_y F_{ris}(\theta_{i,a})$ [28], where d_x and d_y are the length and width of one RIS element, and $F_{ris}(\theta_{i,a})$ represents normalized radiation pattern such that $F_{ris}(\theta_{i,a}) = G_{ris}(\theta_{i,a})/\int_{\phi=0}^{2\pi} \int_{\theta=0}^{2\pi} G_{ris}(\theta) \sin\theta d\theta d\phi$. Nevertheless, the difference in RIS pathloss does not significantly impact the proposed algorithm, since only a constant defined in Eq. (10), which will be introduced in the following part, requires modification to account for a different pathloss model. Based on our simulations using the parameters in Sec. V, only a slight gap in the results is observed from the two different path loss models.

For the radiation pattern $G_{ris}(\theta)$, we use the following model [33] which has been widely used in reflectarrays:

$$G_{ris}(\theta) = 2(2q+1)\cos^{2q}(\theta), \theta \in (-\frac{\pi}{2}, \frac{\pi}{2})$$
 (7)

We pick q=0.5 here, so that $G_{ris}(\theta)=4\cos(\theta), \theta\in$ $\left(-\frac{\pi}{2},\frac{\pi}{2}\right)$. The radiation pattern used in this paper is shown in Fig.2(a).

C. Communication Region and Visible Region

To guarantee the communication performance, the received power at the user should reach a threshold P_{th} , which is dependent on the noise power. The coverage area of an AP is defined as the region where the received power at the user is greater than P_{th} . Then, the coverage area of the AP is a circle with radius $R_a=\sqrt{\frac{P_tG_aG_u\lambda^2}{(4\pi)^2P_{th}}}$. For the ith RIS, the communication distance is

$$R_{ris}(r_{ra}^i, \theta_a^i, \theta_u^i) = \frac{N\lambda^2}{(4\pi)^2 r_{ra}^i} \sqrt{\frac{P_t G_a G_u G_{ris}(\theta_u^i) G_{ris}(\theta_a^i)}{P_{th}}},$$
(8)

where r_{ra}^{i} is the distance from the *i*th RIS to the AP, θ_{a}^{i} is the incident angle from AP to the center of the ith RIS, and θ_u^i is the reflected angle from the center of the ith RIS to the user. To simplify analysis in the rest of the paper, the communication area of the ith RIS is defined as a semicircle, as indicated by the red curve in Fig. 2(b), the radius of which is

$$\tilde{R}_{ris}(r_{ra}^{i}, \theta_{a}^{i}) = \max_{\theta_{u}^{i}} R_{ris}(r_{ra}^{i}, \theta_{a}^{i}, \theta_{u}^{i})$$

$$= C_{r} \frac{\sqrt{G_{ris}(\theta_{a}^{i})}}{r_{-}^{i}}, \tag{9}$$

where

$$C_r = \frac{N\lambda^2}{(4\pi)^2} \sqrt{\frac{P_t G_a G_u G_{ris}(0)}{P_{th}}}.$$
 (10)

Note that the black curve in Fig. 2(b) is the exact boundary of the communication region where received power at the user is greater than P_{th} , and the semicircle is an approximation of it. A performance function will be discussed in Sec. III-D to indicate the signal quality within the semicircle and show the influence of the radiation pattern. The reason we use the approximated communication region is that it simplifies the analysis needed to derive the coverage control algorithm in

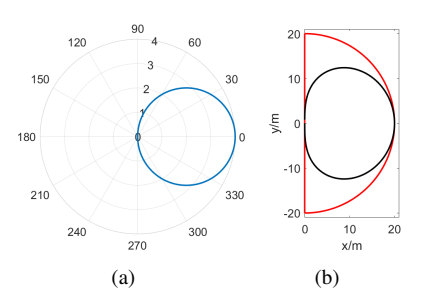


Fig. 2. (a) Radiation pattern $G_{ris}(\theta) = 4\cos\theta$ when q = 0.5; (b) Illustration of communication region of RIS

Sec. IV, and it is easy to generalize when the radiation pattern is defined differently from the one adopted in this paper.

The following concerns the definition of visible regions. Let Q denote the set of all the points in a given scenario that fall outside of obstacles, and O denote the set of points belonging to obstacles. As shown in Fig. 3(a), the ith RIS with state s_i has a limited communication domain C_i modeled as a semicircle region with radius $\tilde{R}_{ris}(r_{ra}^i, \theta_a^i)$, and orientation θ_i , such that [14]

$$C_i = \left\{ \boldsymbol{p} \in \boldsymbol{Q} | \| \theta(\boldsymbol{s}_i, \boldsymbol{p}) \| \le \frac{\pi}{2}, \\ \| \boldsymbol{p} - \boldsymbol{q}_i \| \le \tilde{R}_{ris}(r_{ra}^i, \theta_a^i) \right\}.$$
 (11)

However, when there are obstacles in the scenario, parts of C_i cannot receive signals from the AP. Thus, the visible region V_i is the set containing all the points in C_i that have LoS links to the ith RIS, such that

$$V_i = \{ \boldsymbol{p} \in \boldsymbol{C}_i | \forall \lambda \in [0, 1], \lambda \boldsymbol{p} + (1 - \lambda) \boldsymbol{q}_i \notin \boldsymbol{O} \}.$$
 (12)

An example of V_i is shown in Fig. 3(b).

Finally, the blind region of AP is defined as

$$\boldsymbol{B}_{AP} = \{ \boldsymbol{p} \in \boldsymbol{Q} | \|\boldsymbol{q}_{AP} - \boldsymbol{p}\| > R_a \} \cup \{ \boldsymbol{p} \in \boldsymbol{Q} | \exists \lambda \in [0, 1], \lambda \boldsymbol{p} + (1 - \lambda) \boldsymbol{q}_{AP} \in \boldsymbol{O} \}. \quad (13)$$

where $q_{AP} \in \mathbb{R}^{2 \times 1}$ is the location of AP.

D. Performance Function

The performance function is used to indicate the signal quality in a visible region. A proper performance function should meet the following requirements: (1) the function is differentiable w.r.t. q_i and θ_i within the visible region to meet the calculation requirements in Sec. IV; (2) the function should distinguish between points with received power larger than P_{th} and smaller than P_{th} ; (3) the function is non-increasing as $\frac{G_{ris}(\theta(s_i,p))}{\|p-q_i\|^2}$ decreases for a point $p \in V_i$. Based on the above requirements, the Sigmoid function $Sig(x) = 1/(1 + \exp(-kx))$ is chosen. Then, the performance function at point p is defined as follows

$$f_i(\mathbf{s}_i, \mathbf{p}) = \frac{1}{1 + e^{-kg(\mathbf{s}_i, \mathbf{p})}},\tag{14}$$

where

$$g(\mathbf{s}_i, \mathbf{p}) = W(\mathbf{s}_i, \mathbf{p}) - a(\mathbf{s}_i), \tag{15}$$

$$W(\boldsymbol{s}_{i}, \boldsymbol{p}) = \log_{10} \frac{G_{ris}(\theta(\boldsymbol{s}_{i}, \boldsymbol{p}))}{\|\boldsymbol{p} - \boldsymbol{q}_{i}\|^{2}},$$
(16)

$$a(s_i) = \frac{2.94}{k} + \log_{10} \frac{G_{ris}(0)}{\tilde{R}_{ris}^2(\|\mathbf{q}_i - \mathbf{q}_{AP}\|, \theta(s_i, \mathbf{q}_{AP}))}.$$
 (17)

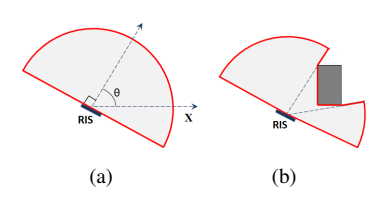


Fig. 3. (a) Communication domain C_i ; (b) Visible region V_i

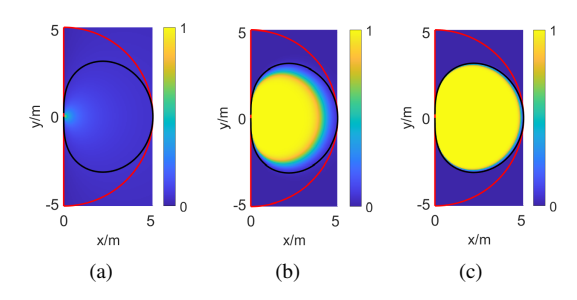


Fig. 4. The distribution of the performance function when (a) k=1, (b) k=20, and (c) k=100.

The term $a(s_i)$ is used to ensure that the coverage performance approaches 0 when the received power is less than P_{th} , and approaches 1 when the received power is greater than P_{th} . The term $\frac{2.94}{k}$ in $a(s_i)$ limits the performance function to be less than 0.05 outside the ideal boundary since $1/(1+\exp(2.94))\approx 0.05$.

Fig. 4 shows different distributions of the performance function at k=1,20, and 100 when the RIS is placed at $[0,0]^T$ with orientation $\theta_i=0$, and the AP is located at $[10,0]^T$. The red curve is the boundary of the communication region C_i and the black curve is the ideal boundary of the region with received power larger than P_{th} . The figures indicate that the value of k describes the transition rate between the region with received power larger than P_{th} and the region with received power smaller than P_{th} . A larger k indicates faster transition rate and approximates the ideal boundary better, but shows less differences among different signal qualities. To reach a balance, we set k=20.

Let $S = [s_1, s_2, ..., s_{N_{RIS}}]$ denote states of all RISs. And let $S_{N_i} = [s_{\pi_1}, s_{\pi_2}, ..., s_{\pi_k}]$ denote the combination of RIS states, where the indexes $\pi_n(n=1,...k)$ all come from N_i . Here, N_i is defined as the index set of all RISs whose visible region intersect with the ith RIS, such that $N_i = \{\pi_n | V_i \cap V_{\pi_n} \neq \emptyset, \pi_n \neq i, \pi_n = 1, ... N_{RIS}\}$. Then, the overall coverage performance function can be defined as

$$H(\mathbf{S}) = \sum_{i=1}^{N_{RIS}} F_i(\mathbf{s}_i, \mathbf{S}_{N_i}), \tag{18}$$

where N_{RIS} is the number of RISs, and $F_i(s_i, S_{N_i})$ is the coverage performance of the *i*th RIS, such that

$$F_i(\boldsymbol{s}_i, \boldsymbol{S}_{N_i}) = \int_{\boldsymbol{V}_i} f_i(\boldsymbol{s}_i, \boldsymbol{p}) \Phi(\boldsymbol{s}_i, \boldsymbol{S}_{N_i}, \boldsymbol{p}) d\boldsymbol{p}.$$
 (19)

In Eq. (19), $\Phi(s_i, S_{N_i}, p)$ is a density function indicating the importance of each point in V_i which will be discussed in Sec. III-E.

E. Density Function

The density function $\Phi(s_i, S_{N_i}, p) \in [0, 1]$ maps a point p in V_i to a positive value in order to show the impact of this point on coverage performance. The function is composed

of two parts: local density $\Phi_l(s_i, S_{N_i}, p)$ and global density $\Phi_q(p)$. Therefore, the density function is defined as

$$\Phi(\boldsymbol{s}_i, \boldsymbol{S}_{N_i}, \boldsymbol{p}) = \Phi_l(\boldsymbol{s}_i, \boldsymbol{S}_{N_i}, \boldsymbol{p})\Phi_q(\boldsymbol{p}). \tag{20}$$

The local density function is used to show the importance of a point $p \in V_i$ when calculating coverage performance contributed by the *i*th RIS. It is defined as follows:

$$\Phi_{l}(\boldsymbol{s}_{i}, \boldsymbol{S}_{N_{i}}, \boldsymbol{p}) = \begin{cases} 1, & \text{if } \boldsymbol{p} \in \boldsymbol{V}_{i} \text{ and } \forall j \in \boldsymbol{N}_{i}, \boldsymbol{p} \notin \boldsymbol{V}_{j}, \\ \frac{f_{i}(\boldsymbol{s}_{i}, \boldsymbol{p})}{\sum_{j \in \{\boldsymbol{N}_{i}(\boldsymbol{p}) \cup i\}} f_{j}(\boldsymbol{s}_{j}, \boldsymbol{p})}, \\ & \text{if } \boldsymbol{p} \in \boldsymbol{V}_{i} \text{ and } \exists j \in \boldsymbol{N}_{i}, \boldsymbol{p} \in \boldsymbol{V}_{j}, \\ 0, & \text{if } \boldsymbol{p} \notin \boldsymbol{V}_{i}, \end{cases}$$

$$(21)$$

where $N_i(p) \subset N_i$ is the index set of all RISs whose visible region intersect with the ith RIS at point p, such that $N_i(p) = \{\pi_n \in N_i | p \in V_i \text{ and } p \in V_{\pi_n}\}$. The goal of this function is to balance coverage performance of different points by assigning a smaller density value to a point covered by more RISs. If all the points had the same density, RISs would likely overlap with each other resulting in some points with high coverage performance while others remain in blind regions, which is contrary to our goal to spread the RISs and cover a given area as much as possible.

The global density $\Phi_g(p)$ is used to show the information of a given scenario, such that a higher density at a point corresponds to a higher need to be covered. Since it is more worthwhile to cover blind regions where there is no LoS link from the AP, the points within blind regions are assigned with a higher density than those outside blind regions, such that

$$\Phi_g(\mathbf{p}) = \begin{cases} 1, \mathbf{p} \in \mathbf{B}_{AP}, \\ 0, \mathbf{p} \notin \mathbf{B}_{AP}. \end{cases}$$
 (22)

F. Coverage Optimization

The goal of the coverage optimization problem is to find optimum RIS locations and orientations to maximize the coverage performance function in order to cover blind regions as much as possible. The problem can be formally stated as follows:

$$\max_{\boldsymbol{S}} H(\boldsymbol{S})$$

$$s.t. \ \forall i = 1, ..., N_{RIS}, \quad \|\theta(\boldsymbol{s}_i, \boldsymbol{q}_{AP})\| \le \frac{\pi}{2} \quad \text{and}$$

$$\lambda \boldsymbol{q}_{AP} + (1 - \lambda)\boldsymbol{q}_i \in \boldsymbol{Q} \backslash \boldsymbol{B}_{AP} \text{ for all } \lambda \in [0, 1].$$
 (24)

The constraints are used to guarantee that there exists a proper link between the AP and each RIS.

IV. COVERAGE EXPANSION BY GRADIENT DESCENT

In this section, a gradient-descent-based algorithm is proposed to optimize the locations and orientations of RISs with the aim to maximize the performance function. The algorithm can be implemented in an indoor scenario with obstacles to maximize the coverage region of the AP.

A. Overall Algorithm

To maximize the coverage performance, each RIS starts from its initialized location and orientation, and then updates its heading direction iteratively moving in the direction that increases the overall coverage performance function $H(\mathbf{S})$. The updating rule is described as follows:

$$q_i(k+1) = q_i(k) + \sigma_k \frac{\partial H(S)}{\partial q_i}(k),$$
 (25)

$$\theta_i(k+1) = \theta_i(k) + \sigma_k \frac{\partial H(S)}{\partial \theta_i}(k),$$
 (26)

where the step size σ_k is chosen using the backtracking line search method at each step [34]. To ensure that there always exists a proper link between the AP and each RIS, we adjust the updated locations and orientations as follows if they do not satisfy constraints (24):

$$q_{i}(k+1) = \underset{\boldsymbol{p} \in \boldsymbol{Q} \backslash \boldsymbol{B}_{AP}}{\operatorname{argmin}} \|\boldsymbol{p} - \boldsymbol{q}_{i}(k+1)\|^{2},$$

$$\operatorname{if} \boldsymbol{q}_{i}(k+1) \in \boldsymbol{B}_{AP} \cup \boldsymbol{O}, \quad (27)$$

$$\theta_{i}(k+1) = \begin{cases} \theta_{\boldsymbol{q}_{i}}(\boldsymbol{q}_{AP}) + \frac{\pi}{2}, & \text{if } \theta_{\boldsymbol{q}_{i}}(\boldsymbol{q}_{AP}) - \theta_{i}(k) < -\frac{\pi}{2}, \\ \theta_{\boldsymbol{q}_{i}}(\boldsymbol{q}_{AP}) - \frac{\pi}{2}, & \text{if } \theta_{\boldsymbol{q}_{i}}(\boldsymbol{q}_{AP}) - \theta_{i}(k) > \frac{\pi}{2}. \end{cases} \tag{28}$$

To make sure that $\theta_i(k+1) \in [-\pi,\pi]$, the orientation will be refined as $\theta_i(k+1) = \mod(\theta_i(k+1) + \pi, 2\pi) - \pi$. The update stops when $\frac{H(\mathbf{S}(k+1)) - H(\mathbf{S}(k))}{H(\mathbf{S}(k))} \le \epsilon_s(\epsilon_s > 0)$.

B. Gradient Derivative

The main issue of the above problem is how to calculate the gradient term $\frac{\partial H(S)}{\partial q_i}$ and $\frac{\partial H(S)}{\partial \theta_i}$. Let $P_i(s_i, S_{N_i}, p) = f_i(s_i, p)\Phi(s_i, S_{N_i}, p)$. By applying differential rules from [13] and [15], we have

$$\frac{\partial H(\mathbf{S})}{\partial \mathbf{q}_{i}} = \frac{\partial F_{i}(\mathbf{s}_{i}, \mathbf{S}_{N_{i}})}{\partial \mathbf{q}_{i}} + \sum_{j \in \mathbf{N}_{i}} \frac{\partial F_{j}(\mathbf{s}_{j}, \mathbf{S}_{N_{j}})}{\partial \mathbf{q}_{i}}$$

$$= \left\{ \int_{\mathbf{V}_{i}} \frac{\partial}{\partial \mathbf{q}_{i}} P_{i}(\mathbf{s}_{i}, \mathbf{S}_{N_{i}}, \mathbf{p}) d\mathbf{p} \right\}$$

$$+ \sum_{\partial \mathbf{q}_{\gamma_{k}} \in l(\mathbf{V}_{i})} \int_{\partial \mathbf{q}_{\gamma_{k}}} D_{i}(\mathbf{s}_{i}, \mathbf{S}_{N_{i}}, \boldsymbol{\gamma}_{k}) \frac{\partial \boldsymbol{\gamma}_{k}}{\partial \mathbf{q}_{i}}^{T} \boldsymbol{n}_{k}(\boldsymbol{\gamma}_{k}) d\boldsymbol{\gamma}_{k} \right\}$$

$$+ \sum_{j \in \mathbf{N}_{i}} \left\{ \int_{\mathbf{V}_{j} \cap \mathbf{V}_{i}} \frac{\partial}{\partial \mathbf{q}_{i}} P_{j}(\mathbf{s}_{j}, \mathbf{S}_{N_{j}}, \mathbf{p}) d\mathbf{p} \right\}$$

$$+ \sum_{\partial \mathbf{q}_{\gamma_{k}} \in l(\mathbf{V}_{j} \cap \mathbf{V}_{i})} \int_{\partial \mathbf{q}_{\gamma_{k}}} D_{j}(\mathbf{s}_{j}, \mathbf{S}_{N_{j}}, \boldsymbol{\gamma}_{k}) \frac{\partial \boldsymbol{\gamma}_{k}}{\partial \mathbf{q}_{i}}^{T} \boldsymbol{n}_{k}(\boldsymbol{\gamma}_{k}) d\boldsymbol{\gamma}_{k} \right\}, \tag{29}$$

where $\boldsymbol{l}(\boldsymbol{V}_i)$ is the set of discontinuity intervals of points in \boldsymbol{V}_i , including boundaries of \boldsymbol{V}_i , boundaries of intersected visible regions and other possible discontinuities within \boldsymbol{V}_i caused by the performance function. Since the performance function defined in this paper is continuous within \boldsymbol{V}_i , $\boldsymbol{l}(V_i)$ only includes boundaries of \boldsymbol{V}_i and boundaries of intersected

visible regions. From [13], in Eq. (29), $n_k(\gamma_k)$ is the normalized outward vector at point γ_k on curve ∂q_{γ_k} , and $D_i(s_i, S_{N_i}, \gamma_k)$ is defined as follows:

$$D_{i}(\boldsymbol{s}_{i}, \boldsymbol{S}_{N_{i}}, \boldsymbol{\gamma}_{k}) = \lim_{\epsilon \to 0^{+}} P(\boldsymbol{s}_{i}, \boldsymbol{S}_{N_{i}}, \boldsymbol{\gamma}_{k} - \epsilon \boldsymbol{n}_{k}) - \lim_{\epsilon \to 0^{+}} P(\boldsymbol{s}_{i}, \boldsymbol{S}_{N_{i}}, \boldsymbol{\gamma}_{k} + \epsilon n_{k}).$$
(30)

The equation for $\frac{\partial F_i(s_i, S_{N_i})}{\partial \theta_i}$ is similar to that of $\frac{\partial F_i(s_i, S_{N_i})}{\partial q_i}$, and can be obtained by replacing ∂q_i with $\partial \theta_i$.

1) Internal gradient within V_i : In the first term of Eq. (29), the derivative is calculated over the entire V_i . We have

$$\frac{\partial P_{i}(\boldsymbol{s}_{i}, \boldsymbol{S}_{N_{i}}, \boldsymbol{p})}{\partial \boldsymbol{q}_{i}}$$

$$= \begin{cases}
\frac{\partial f_{i}(\boldsymbol{s}_{i}, \boldsymbol{p})}{\partial \boldsymbol{q}_{i}}, & \text{if } \boldsymbol{p} \in \boldsymbol{V}_{i} \text{ and } \forall j \in \boldsymbol{N}_{i}, \boldsymbol{p} \notin \boldsymbol{V}_{j}, \\
\Phi_{l}(\boldsymbol{s}_{i}, \boldsymbol{S}_{N_{i}}, \boldsymbol{p}) \left(2 - \Phi_{l}(\boldsymbol{s}_{i}, \boldsymbol{S}_{N_{i}}, \boldsymbol{p})\right) \frac{\partial f_{i}(\boldsymbol{s}_{i}, \boldsymbol{p})}{\partial \boldsymbol{q}_{i}}, & (31) \\
& \text{if } \boldsymbol{p} \in \boldsymbol{V}_{i} \text{ and } \exists j \in \boldsymbol{N}_{i}, \boldsymbol{p} \in \boldsymbol{V}_{j}, \\
0, & \text{other.}
\end{cases}$$

For $j \in N_i$, we have

$$\frac{\partial P_{j}(\boldsymbol{s}_{j}, \boldsymbol{S}_{N_{j}}, \boldsymbol{p})}{\partial \boldsymbol{q}_{i}} = \begin{cases}
-\Phi_{l}^{2}(\boldsymbol{s}_{j}, \boldsymbol{S}_{N_{j}}, \boldsymbol{p}) \frac{\partial f_{i}(\boldsymbol{s}_{i}, \boldsymbol{p})}{\partial \boldsymbol{q}_{i}}, \\
\text{if } \boldsymbol{p} \in \boldsymbol{V}_{i} \cap \boldsymbol{V}_{j}, \\
0, \text{ other,}
\end{cases} (32)$$

where the term $\frac{\partial f_i(s_i,p)}{\partial q_i}$ is easy to calculate. Similarly, the calculation of the derivative w.r.t θ_i can be derived simply by replacing ∂q_i with $\partial \theta_i$ in the above equations.

2) Curve integral over boundaries of V_i : To calculate the curve integrals in Eq. (29), it is required to know the unit outward vector $n(\gamma)$ and the derivatives $\frac{\partial \gamma}{\partial q_i}$ and $\frac{\partial \gamma}{\partial \theta_i}$. Five types of curves related to the *i*th RIS are shown in Fig. 5.

As shown in Fig. 5(a), overlapped boundaries are the boundaries of visible region of neighboring RISs which intersect with V_i . The obstacle boundaries in Fig. 5(b) contain points of fixed obstacles intersected with V_i . These two types of boundaries are irrelevant to parameters q_i and θ_i , so they have no impact on the gradient calculation since $\frac{\partial \gamma_k}{\partial q_i} = 0$ and $\frac{\partial \gamma_k}{\partial \theta_k} = 0$. Only boundaries in Fig. 5(c)-5(e) need to be taken into consideration. For boundaries $\partial q_{oldsymbol{\gamma}_k} \in oldsymbol{l}(oldsymbol{V}_i)$ in Fig. 5(c)-5(e), if γ_k is a point on ∂q_{γ_k} , we have

$$D_i(\boldsymbol{s}_i, \boldsymbol{S}_{N_i}, \boldsymbol{\gamma}_k) = f_i(\boldsymbol{s}_i, \boldsymbol{p}) \Phi_l(\boldsymbol{s}_i, \boldsymbol{S}_{N_i}, \boldsymbol{p}). \tag{33}$$

For a point γ_k on curve $\partial q_{\gamma_k} \in l(V_j \cap V_i)$,

$$D_{j}(\mathbf{s}_{j}, \mathbf{S}_{N_{j}}, \boldsymbol{\gamma}_{k}) = f_{j}(\mathbf{s}_{j}, \boldsymbol{p}) \Phi_{l}(\mathbf{s}_{j}, \mathbf{S}_{N_{j}}, \boldsymbol{p}) - f_{j}(\mathbf{s}_{j}, \boldsymbol{p}) \Phi_{l}(\mathbf{s}_{j}, \mathbf{S}_{N_{\bar{i}}}, \boldsymbol{p}),$$
(34)

where $N_j^{\bar{i}} = \{\pi_n | \pi_n \neq i \text{ and } \pi_n \in \mathbf{N}_j\}.$

i) Arc segment $\partial {m q}_{\gamma_{Arc}}$

The curve segment in Fig. 5(c) is the arc of the sector. The parameterization of it is defined as

$$\gamma_{Arc}(t) = \mathbf{q}_i + \hat{\mathbf{v}}(t) \times \\ \tilde{R}_{ris}(\|\mathbf{q}_i - \mathbf{q}_{AP}\|, \theta(\mathbf{s}_i, \mathbf{q}_{AP})), t \in [\theta_1, \theta_2], \quad (35)$$

where θ_1 and θ_2 define the angle range of the arc segment. Then, the unit outward vector at point $\gamma_{Arc}(t)$ is

$$\boldsymbol{n}_{Arc}(\boldsymbol{\gamma}_{Arc}(t)) = \frac{\boldsymbol{\gamma}_{Arc}(t) - \boldsymbol{q}_i}{\|\boldsymbol{\gamma}_{Arc}(t) - \boldsymbol{q}_i\|} = \hat{\boldsymbol{v}}(t).$$
 (36)

The derivative $\frac{\partial \gamma_{Arc}}{\partial q_i}$ is defined as

$$\frac{\partial \boldsymbol{\gamma}_{arc_i}(t)}{\partial \boldsymbol{q}_i} = \boldsymbol{I} + \hat{\boldsymbol{v}}(t) \frac{\partial \tilde{R}_{ris}(\cdot)}{\partial q_i^T}
= \boldsymbol{I} + \hat{\boldsymbol{v}}(t) [C_1 (\boldsymbol{q}_{AP} - \boldsymbol{q}_i)^T - C_2 \boldsymbol{v}^T(\theta_i)], \quad (37)$$

where $C_1, C_2 \in \mathbb{R}$, such that

$$C_{1} = \frac{3C_{r}\sqrt{\hat{\boldsymbol{v}}^{T}(\theta_{i})(\boldsymbol{q}_{AP} - \boldsymbol{q}_{i})}}{\|\boldsymbol{q}_{AP} - \boldsymbol{q}_{i}\|^{\frac{7}{2}}},$$

$$C_{2} = \frac{C_{r}}{\sqrt{\hat{\boldsymbol{v}}^{T}(\theta_{i})(\boldsymbol{q}_{AP} - \boldsymbol{q}_{i})}\|\boldsymbol{q}_{AP} - \boldsymbol{q}_{i}\|^{\frac{3}{2}}},$$
(38)

$$C_2 = \frac{C_r}{\sqrt{\hat{\boldsymbol{v}}^T(\theta_i)(\boldsymbol{q}_{AP} - \boldsymbol{q}_i) \|\boldsymbol{q}_{AP} - \boldsymbol{q}_i\|^{\frac{3}{2}}}},$$
 (39)

where C_r is defined in Eq. (10). The derivative $\frac{\partial \gamma_{Arc}}{\partial \theta_i}$ is

$$\frac{\partial \boldsymbol{\gamma}_{Arc}(t)}{\partial \theta_i} = \frac{\partial R_{ris}(\cdot)}{\partial \theta_i} \hat{\boldsymbol{v}}(t)$$

$$= C_2 \left(\left[-\sin \theta_i, \cos \theta_i \right] (\boldsymbol{q}_{AP} - \boldsymbol{q}_i) \right) \hat{\boldsymbol{v}}(t). \quad (40)$$

ii) Line segment $\partial q_{\gamma_{LO^+}}$ and $\partial q_{\gamma_{LO^-}}$: The boundaries in Fig. 5(d) are line segments caused by obstacles, the parameterization of which are defined as:

$$\gamma_{LO^{+}}(t) = O_a + t \frac{O_a - q_i}{\|Q_a - q_i\|}, t \in [0, t_1],$$
 (41)

$$\gamma_{LO^{-}}(t) = O_b + t \frac{O_b - q_i}{\|Q_b - q_i\|}, t \in [0, t_2],$$
(42)

where O_a and O_b are the two terminals of the obstacle, t_1 and t_2 are the length of $\partial q_{\gamma_{LO^+}}$ and $\partial q_{\gamma_{LO^-}}$ respectively. The corresponding unit outward vectors are:

$$\boldsymbol{n}_{LO^{+}}(\boldsymbol{\gamma}_{LO^{+}}(t)) = \boldsymbol{R}(\frac{\pi}{2}) \frac{\boldsymbol{q}_{i} - \boldsymbol{Q}_{a}}{\|\boldsymbol{q}_{i} - \boldsymbol{Q}_{a}\|}, \tag{43}$$

$$n_{LO^{-}}(\gamma_{LO^{-}}(t)) = R(-\frac{\pi}{2}) \frac{q_i - Q_b}{\|q_i - Q_b\|}.$$
 (44)

The derivatives are defined as

$$\frac{\partial \boldsymbol{\gamma}_{LO^{+}}(t)}{\partial \boldsymbol{q}_{i}} = \frac{t\boldsymbol{R}(\frac{\pi}{2})(\boldsymbol{O}_{a} - \boldsymbol{q}_{i})(\boldsymbol{O}_{a} - \boldsymbol{q}_{i})^{T}\boldsymbol{R}(\frac{\pi}{2})}{\|\boldsymbol{q}_{i} - \boldsymbol{O}_{a}\|^{3}}, (45)$$

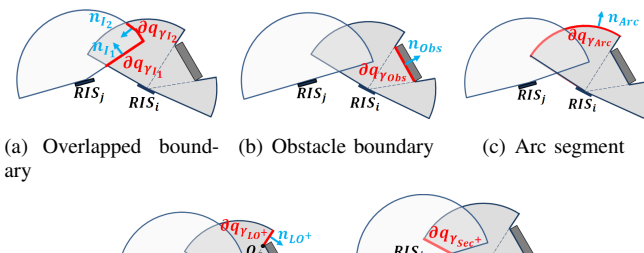
$$\frac{\partial \boldsymbol{\gamma}_{LO^{-}}(t)}{\partial \boldsymbol{q}_{i}} = \frac{t\boldsymbol{R}(\frac{\pi}{2})(\boldsymbol{O}_{b} - \boldsymbol{q}_{i})(\boldsymbol{O}_{b} - \boldsymbol{q}_{i})^{T}\boldsymbol{R}(\frac{\pi}{2})}{\left\|\boldsymbol{q}_{i} - \boldsymbol{O}_{b}\right\|^{3}}, (46)$$

$$\frac{\partial \gamma_{LO^{+}}(t)}{\partial \theta_{i}} = \frac{\partial \gamma_{LO^{-}}(t)}{\partial \theta_{i}} = 0. \tag{47}$$

iii) Line segments $\partial q_{\gamma_{Sec}+}$ and $\partial q_{\gamma_{Sec}-}$ The parametrization of line segments $\partial q_{\gamma_{Sec}+}$ and $\partial q_{\gamma_{Sec}^-}$ illustrated in Fig.5(e) are defined as:

$$\gamma_{Sec^{+}}(t) = \mathbf{q}_{i} + t\hat{\mathbf{v}}(\theta_{i} + \frac{\pi}{2}), t \in [0, r_{1}],$$
 (48)

$$\gamma_{Sec^{-}}(t) = q_i + t\hat{v}(\theta_i - \frac{\pi}{2}), t \in [0, r_2].$$
 (49)



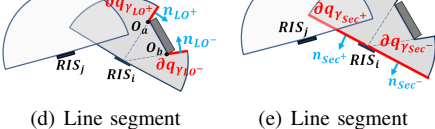


Fig. 5. Illustration of different boundaries and corresponding unit outward vectors

where r_1 and r_2 are the length of $\partial q_{\gamma_{Sec}+}$ and $\partial q_{\gamma_{Sec}-}$ respectively. The corresponding unit outward vectors are

$$m{n}_{Sec^{+}}(\gamma_{Sec^{+}}(t)) = m{R}(\frac{\pi}{2})\hat{m{v}}(\theta_{i} + \frac{\pi}{2}) = -\hat{m{v}}(\theta_{i}), \quad (50)$$
 $m{n}_{Sec^{-}}(\gamma_{Sec^{-}}(t)) = m{R}(-\frac{\pi}{2})\hat{m{v}}(\theta_{i} - \frac{\pi}{2}) = -\hat{m{v}}(\theta_{i}). \quad (51)$

The derivatives are defined as

$$\frac{\partial \gamma_{Sec^{+}}(t)}{\partial q_{i}} = \frac{\partial \gamma_{Sec^{-}}(t)}{\partial q_{i}} = \begin{bmatrix} 1 & 0 \\ 0 & 1 \end{bmatrix}, \quad (52)$$

$$\frac{\partial \gamma_{Sec^{+}}(t)}{\partial \theta_{i}} = -t\hat{\boldsymbol{v}}(\theta_{i}), \tag{53}$$

$$\frac{\partial \gamma_{Sec^{-}}(t)}{\partial \theta_{i}} = t\hat{\boldsymbol{v}}(\theta_{i}). \tag{54}$$

C. Initialization of Gradient Descent

Gradient descent is used for finding a local optimum and final results will be sensitive to the initial locations of RISs. To find a local optimum with better coverage performance, Algorithm 1 is implemented to initialize RIS locations and orientations. The main idea is based on a greedy algorithm where RIS locations are selected one by one from a group of candidate points. In order to tackle the drawback of a greedy algorithm, i.e. that it usually produces a non-optimal result due to its sequential nature, the proposed initialization introduces randomness into each round to provide a better chance of approaching the global optimum over multiple iterations.

As described in Algorithm 1, all the candidate points are divided into two groups, the ones in blinded regions of the AP waiting to be covered by RISs and the ones in the LoS region of AP where RISs can locate. At the beginning of each round, the RIS location is picked from a group of points assigned with different probabilities as in line 7. The probability that a point p can be picked is proportional to the number of blinded points falling into the maximum communication distance of RIS if it is located at p. Then, the RIS orientation is determined by two steps. First, as in line 8, a rough initialization is made by picking one orientation from a small number of candidate angles with number N_a , where the probability of each angle to be picked is proportional to the number of blinded points that the RIS can cover. Second, the final orientation is uniformly selected from a small range of the above picked angle. The blinded points are updated after each RIS is initialized. The process is repeated until the initialization for all RISs is finished. Note that there is still no guarantee that this initialization can lead to the global optimum, but this method provides a reasonable solution that can cover most blind regions and reach good results faster than completely random initialization. This latter point will be demonstrated by numerical simulations in Sec. V.

Algorithm 1 Weighted initialization

```
1: procedure INITIALIZATION(N_{RIS}, N_a)
            Generate the set of uniformly distributed candidate
     points P, and separate P into two sets: P_{nlos} = \{p | p \in
     P,p \in B_{AP}\} and P_{los} = \{p|p \in P, p \notin B_{AP}\}
            Init\_loc \leftarrow \varnothing

    ▶ The set of RIS orientations

            \begin{array}{l} \mathbf{A} = \{-\frac{\pi}{2} + \frac{\pi}{N_{\alpha}}, -\frac{\pi}{2} + \frac{2\pi}{N_{\alpha}}, ..., \frac{\pi}{2} - \frac{2\pi}{N_{\alpha}}, \frac{\pi}{2} - \frac{\pi}{N_{\alpha}}\} \\ \mathbf{while} \ |Init\_loc| < N_{RIS} \ \text{and} \ \mathbf{P_{nlos}} \neq \emptyset \ \mathbf{do} \end{array}
                     Select a candidate point p_k from P_{los}, and the
     probability that a point p_i will be picked is P_{loc}(p_i) =
     |P_{nlos}(p_i)|/\sum_{p_j\in P_{los}}|P_{nlos}(p_j)|, 	ext{ where } P_{nlos}(p_i)=
     \{\boldsymbol{p} \in \boldsymbol{P_{nlos}} | \|\boldsymbol{p_i} - \boldsymbol{p}\| \le \tilde{R}_{ris}(\|\boldsymbol{p_i} - \boldsymbol{q}_{AP}\|, 0)\}
                    Select a candidate angle \alpha_k
     and the probability that \alpha_k will be picked is
     \begin{array}{l} P_{loc}(\boldsymbol{p}_k,\alpha_i) = |\boldsymbol{P_{nlos}}(\boldsymbol{p}_k,\alpha_i)| / \sum_{\alpha_j \in \boldsymbol{A}} |\boldsymbol{P_{nlos}}(\boldsymbol{p}_k,\alpha_j)|, \\ \text{where} \ \ \boldsymbol{P_{nlos}}(\boldsymbol{p}_k,\alpha_i) \ = \ \{\boldsymbol{p}|\boldsymbol{p} \ \in \ \boldsymbol{P_{nlos}}, \|\boldsymbol{p}_k - \boldsymbol{p}\| \ \leq \end{array}
     R_{ris}(\|\boldsymbol{p_k} - \boldsymbol{q}_{AP}\|, \alpha_i, |\theta_{\boldsymbol{p}_k}(\boldsymbol{q}_{AP}) + \alpha_i - \theta_{\boldsymbol{p}_k}(\boldsymbol{p})|)\}
                    Finally, the candidate orientation \theta_k is selected uni-
     formly from [\theta_{p_k}(q_{AP}) + \alpha_k - \frac{\pi}{2N_a}, \theta_{p_k}(q_{AP}) + \alpha_i + \frac{\pi}{2N_a}]
```

```
Init\_loc \leftarrow Init\_loc \cup \{\boldsymbol{p}_k\}
                           Init\_\theta \leftarrow Init\_\theta \cup \{\theta_k\}
11:
                           \begin{aligned} & P_{los} \leftarrow P_{los} \backslash \{p_k\} \\ & P_{nlos} \leftarrow P_{nlos} \backslash P_{nlos}(p_k, \theta_k) \end{aligned}
12:
13:
                 return Init\ loc,\ Init\ \theta
14:
```

V. SIMULATION RESULTS

In this section, numerical simulations are presented to evaluate the proposed coverage expansion algorithm. The parameters used in the simulation are listed in Table I. Here, we simulate 2D cases where the AP, the users, and the centers of RISs are located at the same height. It is also assumed that the AP and users are each equipped with one antenna. For simplicity, the fixed obstacles (e.g. walls, cubicle dividers, or other furniture items) are assumed to be vertical or horizontal line segments.² For weighted initialization, $N_a = 10$ and candidate points uniformly distributed in simulation scenarios are separated by 0.2m. The parameter for stopping criteria of gradient descent is $\epsilon_s = 10^{-4}$.

According to [8], the size of an RIS element is set as $\frac{\lambda}{2}$. The Fraunhofer distance that separates near field and far field is $d_F = \frac{2D^2}{\lambda}$, where D is the maximum linear dimension

²Note that the algorithm also works for polygonal obstacles since a polygonal obstacle can be represented by a set of line segments.

TABLE I SIMULATION PARAMETERS

Parameters	Notations	Values
EIRP for AP	$(P_tG_a)_{dBm}$	40 dBm
Received power threshold	P_{th}	-70 dBm
Antenna gain of users	G_u	0 dB
Number of RIS elements	N	16^{2}
Carrier frequency	f_c	60 GHz

TABLE II RIS OPTIMIZATION RESULTS FOR SCENARIO B

	RIS 1	RIS 2	RIS 3
Initial location	$[0.45, 6.38]^T$	$[3.10, 2.75]^T$	$[7.21, 4.21]^T$
Final Location	$[0.05, 7.79]^T$	$[2.23, 6.61]^T$	$[9.92, 4.62]^T$
Initial orientation	0.15π	-0.07π	-0.78π
Final orientation	0.08π	-0.53π	-0.99π

of the RISs. For a 16×16 RIS, $d_F = \frac{2(\sqrt{N}\lambda/2)^2}{\lambda} = 0.64m$. Therefore, in an indoor scenario, the placement of RISs almost certainly satisfies the far-field assumption adopted herein.

A. Validation of the Proposed Algorithm

For initial validation of the algorithm, simulations are conducted in the two specific scenarios illustrated in Fig. 6 and Fig. 7, which are examples of single-RIS and multi-RIS cases, respectively.

For scenario A in Fig. 6, the targeted room is 8m×6m and the AP is located at $[2,3]^T$. In Fig. 6(a), the right part of the scenario is the blinded region of the AP, which can be covered by a single RIS as shown in Fig. 6(b). The RIS is initialized at $[4.21, 1.21]^T$ with orientation 0.69π , and optimized RIS location is $[4.73, 0.05]^T$ with orientation 0.41π . The coverage ratio increases from 0.5323 to 1 when the RIS is deployed. Scenario B in Fig. 7 shows a multi-RIS case where 5 obstacles are randomly placed in a 10m×8m room, the AP is located at $[5,4]^T$, and 3 RISs are available for deployment. The initial and optimized RIS locations are listed in Table II. The coverage ratio is improved from 0.5732 to 0.9851. In both scenarios, the proposed algorithm shows significant coverage improvement. Moreover, it can be seen from Figures 6(c), 6(d), 7(c), and 7(d) that the proposed performance function captures the coverage ratio well.

Table III shows a comparison of random initialization and the proposed weighted initialization in the above two scenarios. The proposed algorithm runs 10 times for each type of initialization. Then, both the average and the best performance values are calculated. It can be concluded that weighted initialization works more efficiently than random initialization in these two scenarios, because the former method is more likely to initialize RISs in good locations and thus it achieves better results with fewer runs.

B. Coverage Ratio vs. Number of Obstacles

In this section, we provide a more thorough evaluation of our algorithm by simulating its performance for varying

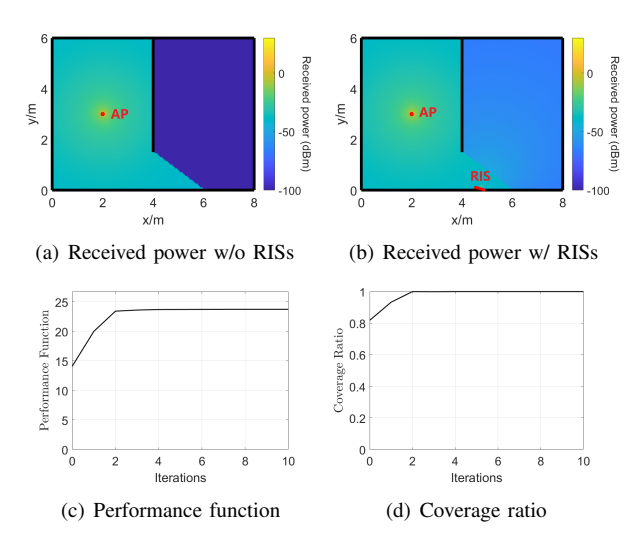


Fig. 6. Simulation results for Scenario A

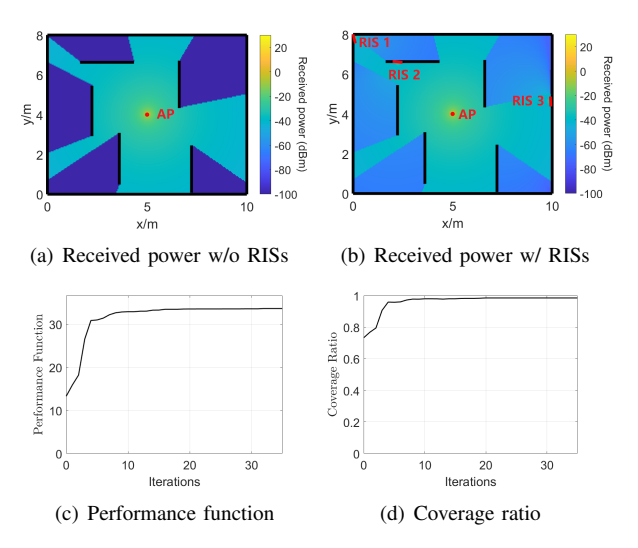
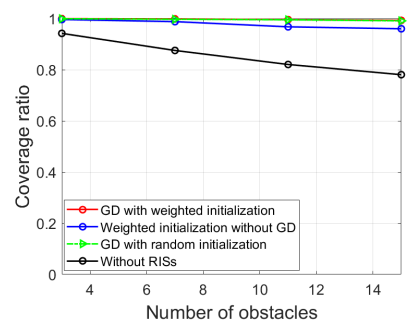


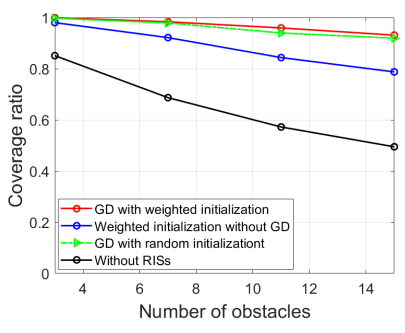
Fig. 7. Simulation results for Scenario B

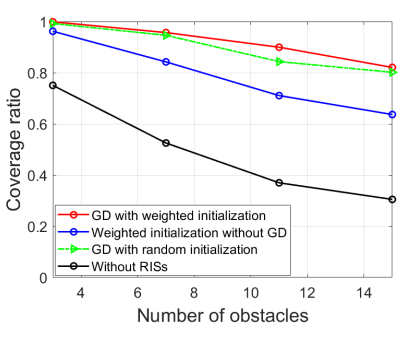
TABLE III COVERAGE PERFORMANCE COMPARISON

	Weighted initialization	Random initialization
Scenario A: Average coverage ratio	0.9974	0.7654
Scenario A: Maximum coverage ratio	1	1
Scenario B: Average coverage ratio	0.9425	0.8931
Scenario B: Maximum coverage ratio	0.9851	0.9827

numbers and lengths of obstacles. In Fig. 8, we compare coverage ratio versus the number of obstacles N_{obs} and expected obstacle length EL. For each combination of N_{obs} and EL, the simulation is run 10 times in each of 8 different obstacle layouts in a 10m×10m room with 3 RISs and the AP located at the center of the room. The maximum coverage ratio is picked out of 10 runs and then the average value across the 8 different random rooms is calculated. The obstacle layouts are chosen randomly as follows: the centers of obstacles are uniformly







- (a) Expectation of obstacle length EL = 0.5m
- (b) Expectation of obstacle length EL = 1.5m
- (c) Expectation of obstacle length EL = 2.5m

Fig. 8. Coverage ratios for different obstacle lengths

distributed across the room and the obstacle length is a random variable with uniform distribution U(0.9EL, 1.1EL). Orientation of each obstacle is randomly set as vertical or horizontal. Results of the proposed gradient descent (GD) algorithm are shown, both with weighted initialization and random initialization. Additionally, weighted initialization but without gradient descent, and performance without RISs are provided as baselines.

First, we note that RISs optimized by the proposed algorithm achieve a significant coverage improvement compared to scenarios without RISs. The coverage ratio reaches 0.99 or higher for EL = 0.5m, and there is a 27% increase relative to the no-RIS scenario when $N_{obs} = 15$ (the obstacles in this setting are not a major hindrance and so the coverage is already relatively high even without RISs). As EL increases, the coverage improvement gets larger. The coverage increase grows to 88% when EL = 1.5m and $N_{obs} = 15$, and is about 170% when EL=2.5m and $N_{obs}=15$. We also note that the gradient descent approach provides much better coverage than the baseline of weighted initialization without gradient descent, which demonstrates the benefits of gradient descent. Finally, weighted initialization demonstrates better coverage compared with random initialization for every combination of EL and N_{obs} , again indicating the efficiency of weighted initialization in reaching better results with fewer runs.

Lastly, a brute force sequential algorithm is used as a comparison to the proposed algorithm. In the brute force sequential algorithm, the best RIS locations and orientations are chosen one by one from "all possible" points and orientations. The candidate points are separated by 0.2m, and candidate orientations are spaced by $\pi/180$. As shown in Fig. 9, when EL = 2.5m, the gradient descent algorithm outperforms the brute force sequential algorithm even with 10 runs, and coverage is improved by about 10% with 50 runs.

For time complexity, since it is not easy to make an accurate analysis of the proposed gradient descent algorithm due to its dependence on the given scenario, a rough comparison will be given based on the number of operations. Here, one operation is defined as all calculations within the communication region of one RIS. In the gradient descent algorithm, one operation includes one search of candidate RIS location and orientation in initialization, and one update of RIS xcoordinate, y-coordinate or orientation in the gradient descent and line search method. In the brute force sequential method, one operation includes one search of candidate RIS location and orientation. When EL = 1.5m, the number of operations of the brute force sequential method is about 65 times as large as in one run of the gradient descent approach, and this grows to about 95 times when EL = 2.5m. Thus, with this approximate analysis, we can see that the gradient descent approach outperforms the brute force sequential approach while executing fewer calculations.

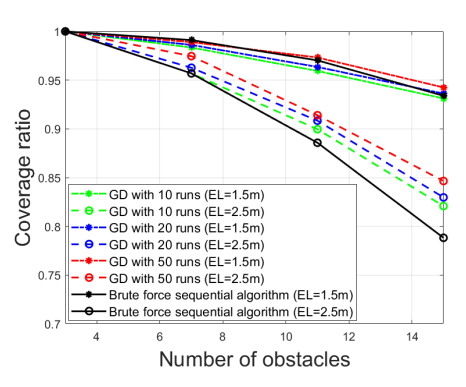


Fig. 9. Comparison of the proposed gradient-descent-based algorithm and brute force sequential algorithm

VI. CONCLUSION

In this paper, we discuss an optimization problem of RIS locations and orientations to expand coverage in the mmWave band. The proposed algorithm is based on gradient descent to maximize a coverage performance function which is carefully selected to incorporate the influence of the RIS radiation pattern. Our simulation results validate that the locations and orientations provided by the algorithm can substantially improve the coverage ratio. The results also show that the proposed weighted initialization can improve efficiency to achieve a satisfying coverage ratio compared with random initialization. To further address the issue of local optima in future work, we plan to evaluate the benefits of incorporating the gradient-descent-based approach into other heuristic optimization algorithms, e.g. a particle swarm algorithm.

REFERENCES

- [1] S. Rangan, T. S. Rappaport, and E. Erkip, "Millimeter-wave cellular wireless networks: Potentials and challenges," *Proceedings of the IEEE*, vol. 102, no. 3, pp. 366-385, 2014.
- [2] T. S. Rappaport, J. N. Murdock, and F. Gutierrez, "State of the art in 60-ghz integrated circuits and systems for wireless communications," Proceedings of the IEEE, vol. 99, no. 8, pp. 1390-1436, 2011.
- A. B. Zekri, R. Ajgou, A. Chemsa, and S. Ghendir, "Analysis of outdoor to indoor penetration loss for mmwave channels," in 020 1st International Conference on Communications, Control Systems and Signal Processing (CCSSP), 2020, pp. 74-79.
- [4] Q. Wu and R. Zhang, "Towards smart and reconfigurable environment: Intelligent reflecting surface aided wireless network," IEEE Communications Magazine, vol. 58, no. 1, pp. 106-112, 2020.
- Q. Wu and R. Zhang, "Towards smart and reconfigurable environment: Intelligent reflecting surface aided wireless network," IEEE Communications Magazine, vol. 58, no. 1, pp. 106-112, 2020.
- [6] C. Liaskos, S. Nie, A. Tsioliaridou, A. Pitsillides, S. Ioannidis, and I. Akyildiz, "A new wireless communication paradigm through softwarecontrolled metasurfaces," IEEE Communications Magazine, vol. 56, no. 9, pp. 162-169, 2018.
- [7] E. Basar, M. Di Renzo, J. De Rosny, M. Debbah, M. Alouini, and R. Zhang, "Wireless communications through reconfigurable intelligent surfaces," IEEE Access, vol. 7, pp. 116753-116773, 2019.
- [8] M. Di Renzo, K. Ntontin, J. Song, F. H. Danufane, X. Qian, F. Lazarakis, J. De Rosny, D. T. Phan-Huy, O. Simeone, R. Zhang, M. Debbah, G. Lerosey, M. Fink, S. Tretyakov, and S. Shamai, "Reconfigurable intelligent surfaces vs. relaying: Differences, similarities, and performance comparison," IEEE Open Journal of the Communications Society, vol. 1. pp. 798-807, 2020.
- X. Tan, Z. Sun, D. Koutsonikolas, and J. M. Jornet, "Enabling indoor mobile millimeter-wave networks based on smart reflect-arrays," in IEEE INFOCOM 2018 - IEEE Conference on Computer Communications, 2018, pp. 270-278.
- [10] P. Wang, J. Fang, L. Dai, and H. Li, "Joint transceiver and large intelligent surface design for massive mimo mmwave systems," IEEE Transactions on Wireless Communications, vol. 20, no. 2, pp. 1052-1064, 2021,
- [11] A. M. Elbir, A. Papazafeiropoulos, P. Kourtessis, and S. Chatzinotas, Deep channel learning for large intelligent surfaces aided mm-wave massive mimo systems," IEEE Wireless Communications Letters, vol. 9, no. 9, pp. 1447-1451, 2020.
- [12] J. Cortés, S. Martínez, T. Karatas, and F. Bullo, "Coverage control for mobile sensing networks," IEEE Transactions on Robotics and Automation, vol. 20, no. 2, pp. 243-255, 2004.
- [13] B. Hexsel, N. Chakraborty, and K. Sycara, "Coverage control for mobile anisotropic sensor networks," in 2011 IEEE International Conference on Robotics and Automation, 2011, pp. 2878-2885.
- [14] H. F. Parapari, F. Abdollahi, and M. B. Menhaj, "Distributed coverage control for mobile robots with limited-range sector sensors," in 2016 IEEE International Conference on Advanced Intelligent Mechatronics (AIM), 2016, pp. 1079-1084.
- [15] J. Cortés, S. Martínez, and F. Bullo, "Spatially-distributed coverage optimization and control with limited-range interactions," ESAIM: COCV, vol. 11, no. 4, pp. 691-719, 2005. [Online]. Available: https://doi.org/10.1051/cocv:2005024
- [16] S. Li, B. Duo, X. Yuan, Y.-C. Liang, and M. Di Renzo, "Reconfigurable intelligent surface assisted uav communication: Joint trajectory design and passive beamforming," IEEE Wireless Communications Letters, vol. 9, no. 5, pp. 716-720, 2020.
- S. Abeywickrama, R. Zhang, Q. Wu, and C. Yuen, "Intelligent reflecting surface: Practical phase shift model and beamforming optimization,' IEEE Transactions on Communications, vol. 68, no. 9, pp. 5849–5863,
- [18] C. Huang, G. C. Alexandropoulos, C. Yuen, and M. Debbah, "Indoor signal focusing with deep learning designed reconfigurable intelligent surfaces," in 2019 IEEE 20th International Workshop on Signal Processing Advances in Wireless Communications (SPAWC), 2019, pp. 1-5.
- [19] A. Taha, M. Alrabeiah, and A. Alkhateeb, "Enabling large intelligent surfaces with compressive sensing and deep learning," IEEE Access, vol. 9, pp. 44304-44321, 2021.

- [20] Q. Wu, S. Zhang, B. Zheng, C. You, and R. Zhang, "Intelligent reflecting surface-aided wireless communications: A tutorial," IEEE Transactions on Communications, vol. 69, no. 5, pp. 3313-3351, 2021.
- [21] B. Xu, T. Zhou, T. Xu, and Y. Wang, "Reconfigurable intelligent surface configuration and deployment in three-dimensional scenarios," in 2021 IEEE International Conference on Communications Workshops (ICC Workshops), 2021, pp. 1-6.
- [22] S. Zeng, H. Zhang, B. Di, Z. Han, and L. Song, "Reconfigurable intelligent surface (ris) assisted wireless coverage extension: Ris orientation and location optimization," IEEE Communications Letters, vol. 25, no. 1, pp. 269-273, 2021.
- K. Ntontin, D. Selimis, A.-A. A. Boulogeorgos, A. Alexandridis, A. Tsolis, V. Vlachodimitropoulos, and F. Lazarakis, "Optimal reconfigurable intelligent surface placement in millimeter-wave communications," in 2021 15th European Conference on Antennas and Propagation (Eu-CAP), 2021, pp. 1-5.
- H. Hashida, Y. Kawamoto, and N. Kato, "Intelligent reflecting surface placement optimization in air-ground communication networks toward 6g," IEEE Wireless Communications, vol. 27, no. 6, pp. 146-151, 2020.
- [25] X. Mu, Y. Liu, L. Guo, J. Lin, and R. Schober, "Joint deployment and multiple access design for intelligent reflecting surface assisted networks," IEEE Transactions on Wireless Communications, vol. 20, no. 10, pp. 6648-6664, 2021.
- X. Liu, Y. Liu, Y. Chen, and H. V. Poor, "Ris enhanced massive nonorthogonal multiple access networks: Deployment and passive beamforming design," IEEE Journal on Selected Areas in Communications, vol. 39, no. 4, pp. 1057-1071, 2021.
- [27] I. Yildirim, A. Üyrus, and E. Basar, "Modeling and analysis of reconfigurable intelligent surfaces for indoor and outdoor applications in future wireless networks," IEEE Transactions on Communications, vol. 69, no. 2, pp. 1290-1301, 2021.
- W. Tang, M. Z. Chen, X. Chen, J. Y. Dai, Y. Han, M. Di Renzo, Y. Zeng, S. Jin, Q. Cheng, and T. J. Cui, "Wireless communications with reconfigurable intelligent surface: Path loss modeling and experimental measurement," IEEE Transactions on Wireless Communications, vol. 20, no. 1, pp. 421-439, 2021.
- T. L. Jensen and E. De Carvalho, "An optimal channel estimation scheme for intelligent reflecting surfaces based on a minimum variance unbiased estimator," in ICASSP 2020 - 2020 IEEE International Conference on Acoustics, Speech and Signal Processing (ICASSP), 2020, pp. 5000-
- [30] Z.-Q. He and X. Yuan, "Cascaded channel estimation for large intelligent metasurface assisted massive mimo," IEEE Wireless Communications Letters, vol. 9, no. 2, pp. 210-214, 2020.
- [31] H. Liu, X. Yuan, and Y.-J. A. Zhang, "Matrix-calibration-based cascaded channel estimation for reconfigurable intelligent surface assisted multiuser mimo," IEEE Journal on Selected Areas in Communications, vol. 38, no. 11, pp. 2621-2636, 2020.
- Q. Wu and R. Zhang, "Beamforming optimization for intelligent reflecting surface with discrete phase shifts," in *ICASSP 2019 2019 IEEE* International Conference on Acoustics, Speech and Signal Processing (ICASSP), 2019, pp. 7830–7833.
- W. L. Stutzman and G. A. Thiele, Antenna theory and design. John Wiley & Sons, 2012.
- [34] L. Armijo, "Minimization of functions having lipschitz continuous first partial derivatives," Pacific Journal of mathematics, vol. 16, no. 1, pp. 1-3, 1966.